Materials Science & Engineering A 910 (2024) 146905

Contents lists available at ScienceDirect

Materials Science & Engineering A

journal homepage: www.elsevier.com/locate/msea

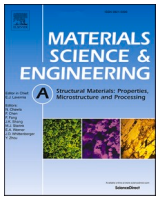

Synthesis, microstructure and micro-mechanical characterization of metal (Nb, Ti) – MAX phase (Ti_2AlC) nanolaminates

Skye Supakul [a], Manish Jain [b], Krishna Yaddanapudi [c], Jacob Gruber [d], Osman El-Atwani [e], Garritt J. Tucker [d,f], Siddhartha Pathak [a,*]

[a] Materials Science and Engineering Department, Iowa State University, IA, 50011, USA
[b] Sandia National Laboratories, Albuquerque, NM, 87185, USA
[c] Department of Materials Science and Engineering, University of California, Davis, CA, 95616, USA
[d] Materials Science Program, Colorado School of Mines, Golden, CO, 80401, USA
[e] Reactor Materials Group, Pacific Northwest National Laboratories, Richland, WA, 99354, USA
[f] Department of Physics, Baylor University, Waco, TX, 76706, USA

ARTICLE INFO

Keywords:
Multilayers
Nanocomposite
MAX phase
PVD
Microcompression
Nanoindentation
TEM

ABSTRACT

We utilize elevated temperature physical vapor deposition (PVD) techniques to design metal/MAX multilayered nanocomposite thin films with alternating nanoscale metallic (Nb, Ti) and MAX phase (Ti_2AlC) layer thicknesses. These metal/MAX nanolaminate architectures attempt to exploit a unique hierarchical topology – as interfaces between the layers are expected to be in direct competition with the internal interfaces within the MAX layers, to drive their tunable macroscopic mechanical behavior. Two metal/MAX nanolaminates – Nb/Ti_2AlC and Ti/Ti_2AlC – were deposited. The Nb/Ti_2AlC metal/MAX system showed highly diffused layer interfaces with distinct Ti – rich and Nb–Al – rich layers, with the presence of MAX phase alongside TiC and other Ti–Al and Nb–Al intermetallic phases. The Nb/Ti_2AlC system possessed a layered architecture, though the MAX phases were not found to be continuously present in each alternating layer. The second Ti/Ti_2AlC system showed a non-lamellar nanocomposite microstructure and the formation of mixed $Ti_{n+1}AlC_n$ phases (a mix of n = 1, 2), and no indication of layering. Diffusion occurring between the metal/MAX layers in both cases, likely due to the elevated temperatures during the deposition process, is speculated as the likely cause of these resultant microstructures. The mechanical properties of both systems were evaluated using micromechanical (nanoindentation and micropillar compression) techniques, which demonstrated high strengths for both systems (Nb system: yield and instability strengths of 4.88 ± 0.1 GPa and 5.57 ± 0.03 GPa, Ti system: yield and instability strength of 5.61 ± 0.28 GPa and 6.21 ± 0.25 GPa). This work highlights the promising mechanical properties of metal/MAX multilayered depositions and summarizes the challenges in PVD synthesis of metal/MAX multilayered nanolaminates.

1. Introduction

Multilayered materials have seen growing attention as a systematic design of materials with favorable mechanical and chemical properties, for applications in extreme temperatures, mechanical loading, and environmental conditions [1–4]. With advances in deposition techniques (e.g., physical vapor deposition (PVD) and chemical vapor deposition (CVD)), microstructural characterization, and micromechanical testing, more and more research is focused on exploring novel multilayered nanocomposite designs [3,5–13]. In particular metal/ceramic multilayers have gained interest recently due to their promising mechanical, physical and chemical properties, making them useful in a wide range of temperatures, mechanical loadings, and environmental conditions [14–18]. One primary scientific interest stems from the large difference in strength and ductility between their constituent phases. However, compared to metal/metal multilayered systems that show significantly higher strength and ductility relative to their non-layered counterparts [19–21], metal/ceramic nanolaminate systems have demonstrated limited improvements in their mechanical properties. In general, the mechanical properties of metal/ceramic composites have lower strengths when compared to their ceramic component and a lower ductility than the metal component [14,17,22,

* Corresponding author. BP Hoover Hall, 528 Bissell Rd, Department of Materials Science and Engineering, Iowa State University, Ames, IA, 50011, USA.
E-mail address: pathak@iastate.edu (S. Pathak).

https://doi.org/10.1016/j.msea.2024.146905
Received 7 February 2024; Received in revised form 27 June 2024; Accepted 29 June 2024
Available online 29 June 2024

23], likely due to the unfavorable transmission of dislocations between the metal and ceramic layers, and a high lattice friction stress on most slip systems of the ceramic component at low homologous temperatures [4,5,24,25]. The ceramic component in these multilayers can be either amorphous [4,5,17,25,26] or crystalline. Better overall material performance, such as higher strength, high work hardening and formability, has been observed in the case of crystalline metal/ceramic multilayer systems, such as Al/TiN [27–30] and Cu/TiN [31]. Such improvements in strength and ductility in the crystalline metal-ceramics nanolaminates has been ascribed to plastic co-deformation mechanisms [32], which become operative as the bilayer thicknesses are reduced to a few nanometers [29,33].

In this work, we build upon these ideas by utilizing alternating metallic and MAX phase depositions to design a metal/MAX multilayered nanocomposite with layer thicknesses reduced to the nanoscale. MAX phases represent a novel class of intrinsic layered solids, where $M_{n+1}X_n$ layers are interleaved with pure A-group element layers (see Fig. 1). The MAX phase family of ceramic materials consist of laminated ternary carbide or nitride materials with the general formula $M_{n+1}AX_n$, where n = 1, 2, or 3, M is an early transition metal; A is an A-group element (a subset of groups 13–16); and X is C and/or N [34–37]. The intrinsic internal layering in the MAX phases offers several unique and advantageous features, which can be exploited for enhanced strength and toughness in a multilayered composite. For example, they exhibit fully, and spontaneously reversible stress-strain hysteresis loops when cyclically loaded in compression, both at the macro- and micro-scales [35,38]. Thus, our efforts to incorporate MAX phase and metal layers into a nanolaminate architecture in this work attempts to exploit a unique hierarchical topology – as interfaces between the layers are expected to be in direct competition with the internal interfaces within the MAX layers, to drive the tunable macroscopic mechanical behavior. A computationally generated model of the proposed hierarchical metal-MAX nanocomposite system is shown in Fig. 1a and b, and the internal layering of the Ti_2AlC MAX phase layer is detailed in Fig. 1b, highlighting the Ti–C layers interfaced with Al layers.

The synthesis and subsequent microstructural and micro-mechanical characterization of two metal/MAX nanolaminates – Nb/Ti_2AlC (the Nb system, Fig. 1c) and Ti/Ti_2AlC (the Ti system, Fig. 1d) – are detailed in this work. Ti_2AlC was chosen as the ceramic MAX phase component of the metal/MAX nanolaminate system due to its ease of deposition, prior success in thin film synthesis using direct current (DC) magnetron sputtering PVD [36], and having been well-studied for various applications in literature [39–41]. For the metallic layer, two metals were investigated: Nb and Ti. Niobium was chosen due to its high melting point and its ability to be deposited using PVD under similar deposition temperatures (800°C-1000 °C) [21]. Titanium was chosen also explored as the metallic layer, to investigate the effect of having the same element (Ti) in both the metallic layer and the early transition metal "M" component of the MAX phase which may impart a further diffuse nature to the metal/MAX interface which can be advantageous for crack tip blunting. PVD was chosen due to its unique advantages in depositing metal/metal and metal/ceramic multilayered laminate architectures [21,31] such as, precise control over both density and length scales of deposition, where the individual layer thicknesses can vary from 2 nm to ~10 μm, the ability to induce epitaxy in the deposited layers, which in turn can help to tune specific interface configurations between the MAX and the metal phases, and flexibility due to the individual control of the elemental fluxes. For Ti_2AlC MAX phase, successful PVD deposition has been observed at temperatures as low as 550 °C [42,43], however higher temperatures of 700 °C–900 °C [44] are generally recommended to encourage the textured epitaxial growth of MAX phase Ti_2AlC [42, 44–47]. Thus, in this work, we explore and discuss preliminary investigations to synthesize epitaxial hierarchical metal (Nb, Ti)/MAX phase (Ti_2AlC) multilayered nanolaminates at elevated temperatures and their resulting microstructures and mechanical properties.

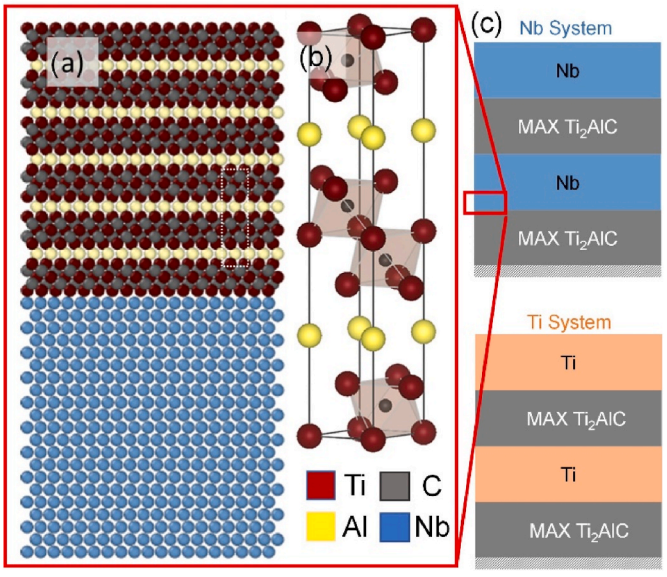

Fig. 1. (a) Computational model of Ti_2AlC MAX phase and metal Nb multilayer with the MAX basal planes parallel to the metal/MAX interface. (b) Internal layering of the Ti_2AlC MAX phase unit cell. Schematic of the two metal/MAX nanolaminates – (c) Nb/Ti_2AlC and (d) Ti/Ti_2AlC – discussed in this work.

2. Materials and methods

Nonlaminated Ti_2AlC thin films (Fig. 2) were deposited in a hybrid sputtering-evaporation PVD chamber (AJA International, Inc., Scituate, Massachusetts) at the Center for Integrated Nanotechnologies (CINT) at Los Alamos National Laboratory (LANL) from elemental targets of Ti, Al, and C sputtering targets of commercial purity at 900 °C. DC magnetron sputtering of the targets involved 80 W, 20 W, and 300 W of power for the Ti, Al, and C targets, respectively. The chamber base pressure was ~2.67×10^{-8} mbar, similar to other reports in literature [45,47–51]. The total film thickness was measured to be ~520 nm.

For the multilayered deposition of the Nb system, the Ti_2AlC MAX phase was deposited using the same conditions as described above, and the Nb layers were deposited at 300 W. Alternate layers of 30 nm thick Ti_2AlC and 30 nm thick Nb were deposited onto the $(11\bar{2}0)$ (i.e., the *a*-plane) of a sapphire Al_2O_3 single crystal substrate. The deposition rates were ~0.25 nm/s for Ti_2AlC and ~0.22 nm/s for Nb. The total film thickness for this system is approximately 680 nm as measured through post-deposition TEM micrographs. For the multilayered deposition of the Ti system, the deposition was conducted in the same chamber and under similar conditions as the Nb system, except that a lower deposition temperature of 800 °C was used. The deposition rate was ~0.25 nm/s for Ti_2AlC and 0.09 nm/s for Ti. The total film thickness for this system was ~4.28 μm as measured using post-deposition SEM micrographs.

Deposited films were characterized with x-ray diffraction (XRD) using a RIGAKU X-ray diffractometer to identify the presence of Nb and Ti_2AlC MAX phases in the deposited layers. Both Bragg-Brentano (BB-XRD) diffracted beam and grazing incidence (GI-XRD) parallel beam XRD were used to identify some of the phases present in the film. Due to the high substrate signal when performing BB-XRD on the Ti system deposition, GI-XRD was used and reported here to minimize the signal coming from the substrate and allow for a larger fraction of signal to come from the film. To examine the local structure and composition, cross-sectional TEM samples of the as-deposited films were prepared using FEI Scios dual-beam focused ion beam (FIB) equipped with Ga^+ source. The samples were then investigated using JEOL JEM 2100F-AC STEM/TEM coupled with energy dispersive spectroscopy (EDS).

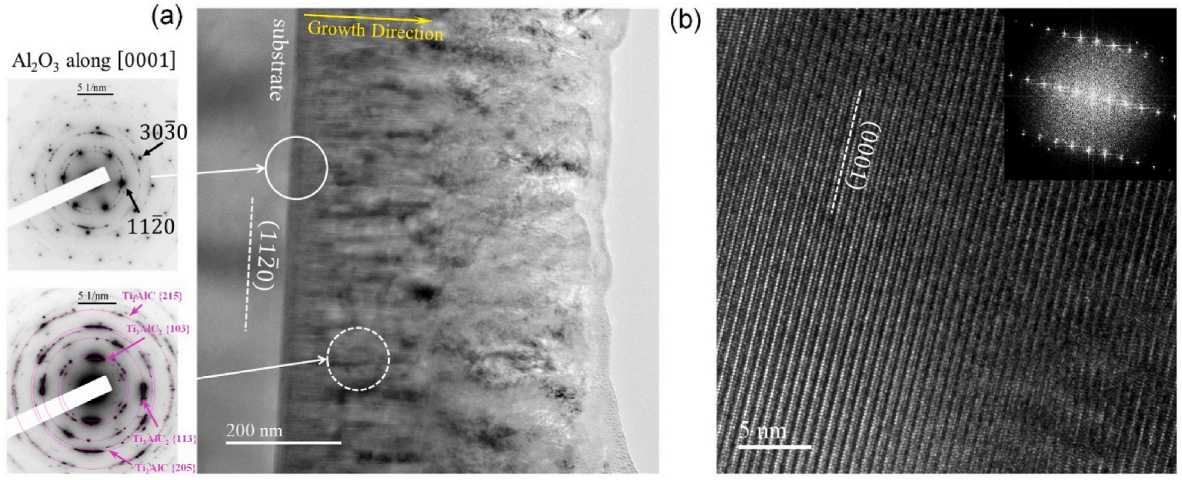

Fig. 2. (a) Brightfield TEM and (b) HR-TEM micrographs showing the microstructure of (non-laminated) Ti_2AlC film deposited on an a-plane sapphire with columnar growth. The broadened diffraction spots in the SAED pattern suggests that the Ti_2AlC is highly textured in (a). The HR-TEM micrograph in (b) shows the atomic layered structure of the Ti_2AlC MAX phase along the $\langle 10\bar{1}0 \rangle$ orientation as evidenced by the FFT pattern.

Hardness and modulus measurements were conducted using a diamond Berkovich tip (manufacturer Synton-MDP, Switzerland) using two nanoindentation instruments – the Hysitron Triboindenter™ and the KLA Nanoindenter G200™. For the Nb system, tests in each machine consisted of 10 s (loading) – 10 s (hold) – 10 s (unloading) cycle to maximum depths of 200 nm and 400 nm. Tests using the KLA Nanoindenter G200™ were performed with and without continuous stiffness measurements (CSM) [52–54] to check for fatigue related effects due to the CSM dynamic loading [55]. To evaluate the thermal stability of the metal and MAX phase layers of the Nb system (Figs. 3–8), samples were exposed to annealing temperatures of 1000 °C for 1 h, and then allowed to cool down to room temperature. This temperature corresponds to $1.36(T_m)_{Al}$, $0.46(T_m)_{Nb}$, $0.65(T_m)_{Ti}$, $0.36(T_m)_{C}$, where T_m is the homologous temperature for the corresponding phase. Hardness and modulus measurements were conducted before and after the thermal treatments.

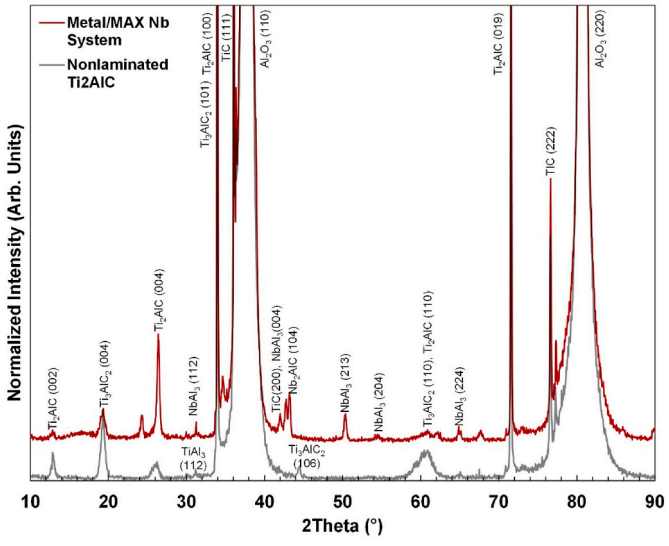

Fig. 3. X-Ray diffraction of two specimens; nonlaminated Ti_2AlC MAX phase thin film (gray) and the Nb/Ti_2AlC metal/MAX system deposited with (targeted) alternating 30 nm layers of Ti_2AlC and Nb layers (red) onto Al_2O_3 $(11\bar{2}0)$ substrate. The presence of MAX phase $Ti_{n+1}AlC_n$ peaks suggest a promising deposition, though there are additional peaks of mixed Nb–Al phases which also suggest the presence of intermetallic phases. (For interpretation of the references to colour in this figure legend, the reader is referred to the Web version of this article.)

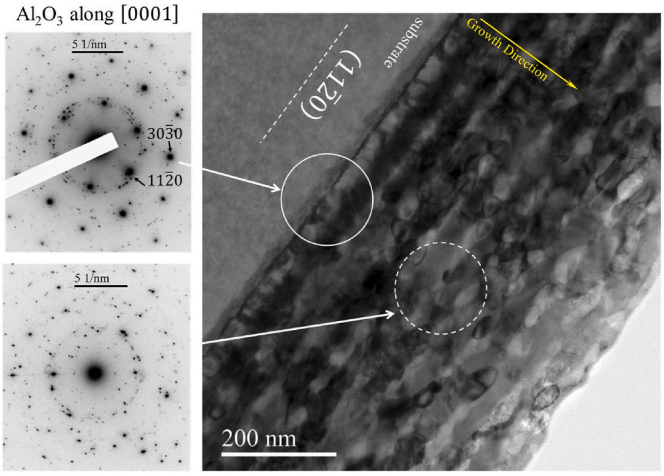

Fig. 4. A cross-sectional TEM micrograph of the as deposited metal/MAX nanolaminate along with the SAED patterns. The solid white circle corresponds to the region where the associated SAED was taken. The well-defined randomly distributed diffraction spots in the SAED pattern acquired from a region enclosed by a dashed white circle indicate the polycrystalline nature of the deposited multilayers.

For the Ti system (Figs. 9–11), only room temperature tests were conducted using the KLA Nanoindenter G200™ to target displacement of 500 nm at 0.05 s^{-1} strain rate with CSM (2 nm amplitude and 45 Hz frequency).

Micropillars were fabricated using a FEI Scios DualBeam SEM/FIB equipped with Ga^+ source. For the Nb system, five micropillars were fabricated and had an effective height-to-diameter ratio of 1:1.17 (~0.68 μm: ~0.8 μm). The micro-pillars were fabricated in such a way so as to ensure that the film-substrate interface is visible during the in-situ SEM experiments. This arrangement allows for accurate measurement of the pillar height and compression strain, as well as correcting for the elastic deformation of the single crystal Al_2O_3 substrate and any associated pillar sink in effects using the procedures described in Ref. [56]. In-situ testing was conducted using two different in-situ nanomechanical testing devices. For the Nb system, micropillars were compressed using the Alemnis Standard Assembly Nanoindenter™ with a constant loading and unloading rate of 2 nm/s to prescribed displacements of 50, 70, and 100 nm using a conductive diamond flat

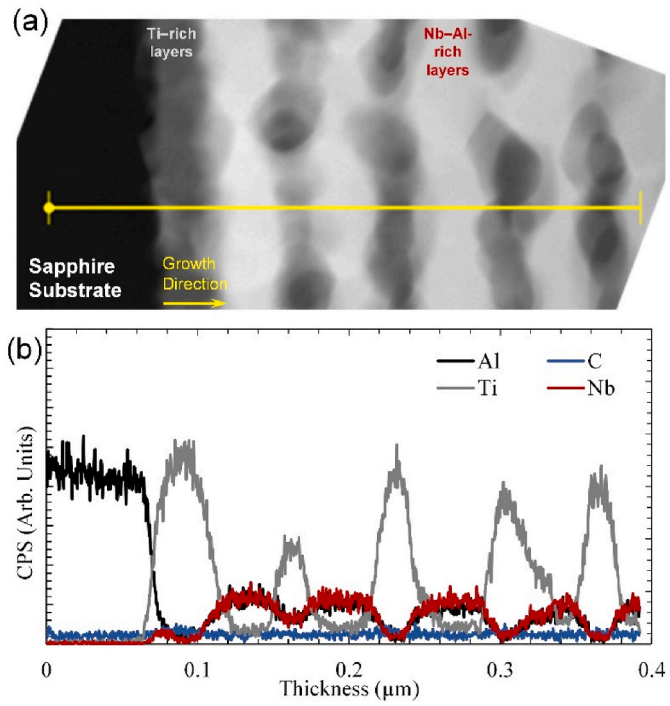

Fig. 5. (a) A dark-field STEM image of the Nb system near the Al_2O_3 substrate with (b) an associated EDS compositional profile. Layer pinch-off can be observed in the STEM image and a high intensity is observed in what is expected to be the Nb layer, supporting the presence of Nb–Al intermetallic phases previously observed in the XRD measurements.

punch indenter. For the Ti system, eleven micropillars were fabricated with a height-to-diameter aspect ratio of 1.4:1 (~4.28 μm: ~3 μm) which were compressed using a Hysitron PI-85 Picoindenter with a constant loading rate of 10 nm/s to varying total strain levels using a conductive diamond flat punch indenter. For the Ti system, the continuously captured image scans were recorded as a video file during the test (see Supplementary videos V1).

We note that the above micro-pillar height-to-diameter ratios (1:1.17 and 1.4:1 for the Nb and Ti systems respectively) are lower than the ideal ratios (2:1 to 3:1) needed to ensure a uniaxial stress state in the pillar [57]. These lower ratios were necessitated due to the small (~680 nm) film thickness of the Nb system thin film. Fabricating the recommended 2:1 to 3:1 height-to-diameter aspect ratios would require a significantly smaller pillar diameter of ~340 nm or even smaller, which can lead to a number of issues such as enhanced taper in the pillar, possible pillar size effects due to decreased dimensions, increased relative ratio of the FIB damaged volume in the pillar that can adversely affect the experimental results, enhanced misalignment issues during the tests etc. Hence the pillar aspect ratios were kept similar (1:1.17 vs. 1.4:1) so that the results between the Nb and Ti systems can be compared to one another.

Factors such as the misalignment between the top of a micropillar and the indenter tip, friction between the indenter tip and the top surface of the micropillar, micropillar taper and edge round-over, micropillar base filet, etc.can cause deviations from the perfect ideal uniaxial test. Effects of taper can be minimized through careful pillar fabrication. Corrections such as substrate effects and pillar sink-in can be accounted for by various equations [56,58], though these corrections affect the effective strain, rather than the effective stress levels and general deformation of the thin film in question. Other aspects such as friction, substrate effects, misalignment, pillar base fillet have also been discussed both in observed in modeling and simulations [57,59] and combined experimental/modeling [12,56,60]. For hard and highly elastic substrates such as the Al_2O_3 single crystals used here, we do not expect any plastic deformation at the stress and strain levels used in this work. The experiments and values shared here in this work are for comparative studies for other thin films with similar complex microstructures and pillar parameters.

3. Results

3.1. Non-laminated Ti_2AlC thin film

To ascertain the parameters for MAX phase deposition, a (non-laminated) Ti_2AlC MAX phase thin film was deposited on a single crystal Al_2O_3 $(11\bar{2}0)$ plane (see **Materials and Methods**). This deposition was characterized with XRD (Fig. 3, gray) with distinct Ti_2AlC peaks at 12.85°, 26.15°, 71.6° which corresponds to (002), (004), and (019). Some of these phases were also observed via TEM investigations as seen in Fig. 2. It should be noted that we also see distinct peaks of Ti_3AlC_2 MAX phase at 19.25°, 44.55° corresponding to (004) and (106) in Fig. 3, indicating that the film is not phase pure Ti_2AlC. Brightfield TEM micrographs in Fig. 2a reveal the columnar growth of the film. Selected area electron diffraction (SAED) taken at the film and substrate interface (Fig. 2a, top left) reveals well defined diffraction spots corresponding to Al_2O_3 for the [0001] direction as well as signatures of a polycrystalline film. Additionally, from the SAED pattern, the position of the $(11\bar{2}0)$ reflection confirms that the film was deposited on the $(11\bar{2}0)$ plane of Al_2O_3. The ring patterns and the broadening of associated diffraction spots in the SAED pattern acquired from a region of the film indicate the textural nature of Ti_2AlC. Indexing of the polycrystalline diffraction rings match well with 312 and 211 $Ti_{n+1}AlC_n$ MAX phase. The subsequent high-resolution (HR) TEM analysis coupled with the FFT analysis reveals the stacking of basal planes of MAX phase Ti_2AlC along the $\langle 10\bar{1}0\rangle$ direction. All of these combined suggest that we are able to successfully deposit MAX phase Ti_2AlC via DC magnetron sputtering PVD.

3.2. Nb system: microstructural characterization

XRD profiles obtained from the multilayered deposition of alternate layers of Nb and Ti_2AlC (the Nb system) are shown in Fig. 3 (red curves). Distinct peaks of MAX phases Ti_2AlC and Ti_3AlC_2 have been identified, suggesting the presence of MAX phase in the deposited film [45,46,49,61,62]. The presence of Nb_xAl_y intermetallic phases were also identified, signifying the presence of Nb, though no peaks corresponding to pure Nb could be identified [63–66]. TiC was also detected with distinct peaks noted. Preliminary SEM imaging (not shown here) suggested the presence of a multilayered architecture.

TEM investigations of the local microstructure and phases present in the Nb system are shown in Figs. 4–6, which appear to consist of discrete alternating layers exhibiting high interface roughness. The blurred interfaces in these figures may indicate the occurrence of diffusion, most likely during the PVD deposition. Fig. 4 shows the microstructure of the as-deposited Nb-metal/MAX multilayered structure deposited on the a-plane Al_2O_3. The corresponding SAED pattern acquired from the substrate/film interface (indicated by a solid white circle) confirms the same orientation of the substrate as evident by a $(11\bar{2}0)$ reflection (indicated by a black arrow) of sapphire substrate. Moreover, the well-defined and randomly distributed non-Al_2O_3 diffraction spots in the SAED pattern suggests that the film deposited is highly polycrystalline, which is further confirmed by the SAED pattern acquired from a region enclosed by the dashed white circle in the film. This corroborates the XRD profile shown in Fig. 3, red, where several diffraction peaks reflect the polycrystalline nature of the sample.

To examine the atomic constituents of the deposited layers, a line EDS scan was performed across the dark-field STEM image as shown in Fig. 5. The Al_2O_3 substrate can be identified as the darkest layer component on the far left, which is in good agreement with the Al-signal in the EDS profile. The Al profile drops down to zero at the substrate/film interface. The EDS line profile corresponding to Al reaches its

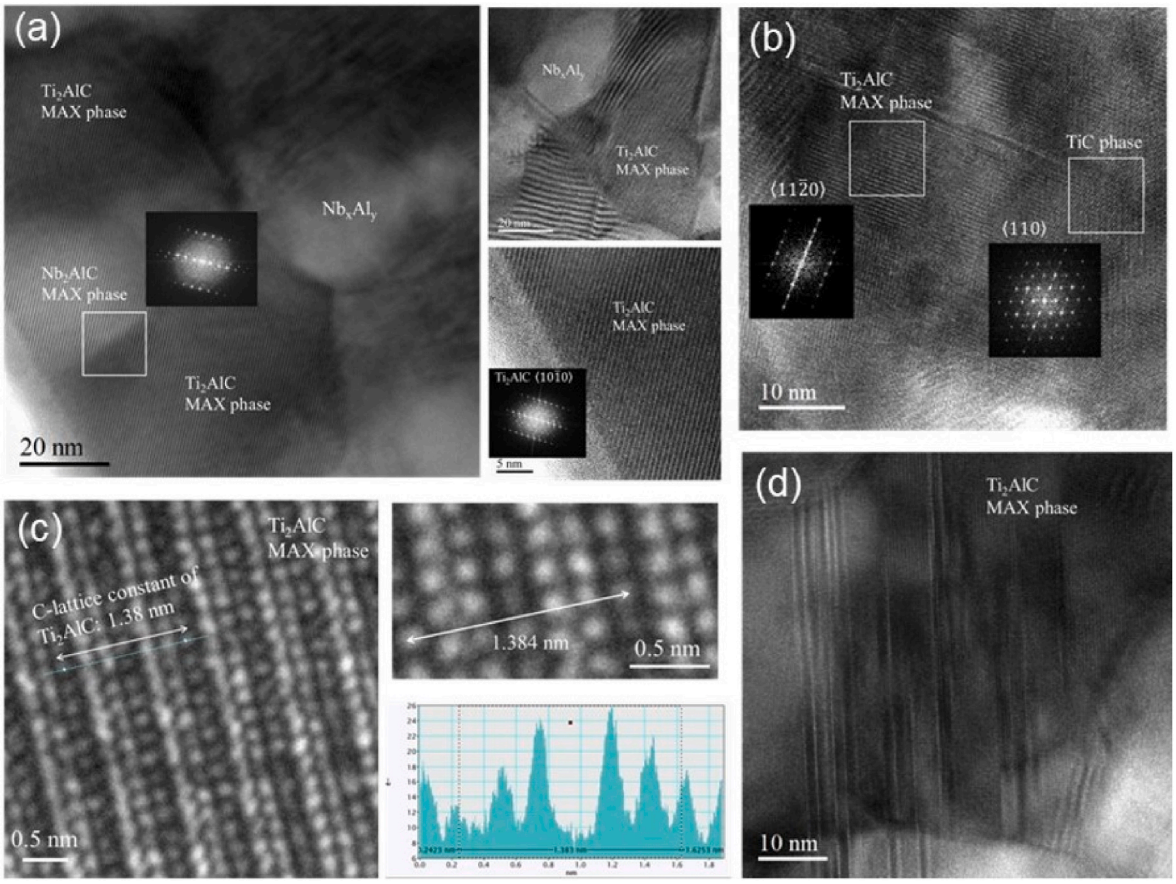

Fig. 6. (a) HR-TEM images of the as deposited Nb composite system showing the signature of Ti_2AlC and Nb_2AlC MAX phases. The FFT patterns are consistent with the $\langle 10\bar{1}0 \rangle$ orientation of the MAX phase. (b) shows the presence of TiC and Ti_2AlC phases adjacent to each other. (c) shows the atomic layered structure of the Ti_2AlC MAX phase. (d) shows the planar faults in the Ti_2AlC MAX phase.

minimum value in the Ti-rich regions and its maximum value in the Nb-rich regions. From the EDS profile the subsequent alternating bright and dark layers were identified to be Nb_xAl_y and Ti-rich regions. To extract the approximate composition of the Nb_xAl_y intermetallic, several EDS line scans were performed in the Nb_xAl_y regions, and the extracted compositions analyzed, showing an increased concentration of Al in the Nb-rich regions, while a low concentration of Al exist in the Ti-rich regions. Furthermore, there is a consistent higher concentration of 4:1 of Al compared to Nb present in the Nb-rich regions. The results indicate that instead of pure Nb, the as-deposited sample consists of an intermetallic Nb_xAl_y compound, probably $NbAl_3$ as identified from the XRD profiles in Fig. 3. The average individual thicknesses of the Nb_xAl_y and Ti-rich layers were measured to be 32.2 ± 0.7 nm and 29.5 ± 0.8 nm, respectively.

As previously observed in both brightfield TEM (Fig. 4) and STEM (Fig. 5) micrographs, the morphology of the film consists of extensively diffused layers with distinct Ti – rich and Nb–Al – rich regions. To gain some insight of some of the phases present in the film, the local structure and phases were examined using HR-TEM (Fig. 6). These investigations confirm the presence of both the Ti_2AlC and Nb_2AlC MAX phases in local isolated regions of the sample. The FFT analysis is consistent with the $\{10\bar{1}0\}$ orientation of Ti_2AlC MAX phases. Further HR investigations in Fig. 6b shows that the atomic layered structure of the Ti_2AlC MAX phase and the extracted 'c' lattice constant (1.38 nm) are in excellent agreement with reported values of the Ti_2AlC lattice constant (1.36 nm) [40,62]. In some regions the TiC phase also has been observed adjacent to the Ti_2AlC MAX phase as indicated by the FFT patterns in Fig. 6c. Planar faults in the Ti_2AlC MAX phase can also be identified in Fig. 6d. Earlier, Fig. 5 presented Ti- rich regions which lacked Al within the layers which suggests that $Ti_{n+1}AlC_n$ is likely not present throughout entirety of the Ti – rich layers. Considering the HR-TEM micrograph in Fig. 6d and the XRD measurements (Fig. 3), it is likely that the Ti – rich layers consist of patches of $Ti_{n+1}AlC_n$ and TiC. Meanwhile, the Nb–Al – rich layers likely consist of mixed $Nb_{n+1}AlC_n$ and Nb_xAl_y phases as observed in Fig. 6a.

3.3. Nb system: nanoindentation and micropillar compression

To evaluate the thermal stability of the deposited thin films, nanoindentation modulus and hardness measurements were conducted using a Berkovich indenter before and after annealing at 1000 °C for 1 h on both the Nb composite system as well as the (control) $Ti_{n+1}AlC_n$ MAX phase thin film (Fig. 7). The as-deposited indentation modulus (254.1 ± 14.0 GPa) and hardness (10.78 ± 1.36 GPa) for the non-laminated Ti_2AlC thin film are similar to those seen in other literature (modulus 240–277 GPa, hardness ~10.1–11.87 GPa [40,80,81]), which indicates a successful deposition of the high density MAX phase specimen. The Nb composite system shows higher elastic modulus (292.5 ± 8.9 GPa) and hardness (16.02 ± 0.42 GPa) values in comparison to the MAX phase Ti_2AlC are observed (Fig. 7a and b), which is to be expected due to the presence of the stiffer and harder TiC component in the multilayers [82,83]. The improved properties of the Nb system can be attributed to (a) the composite architecture of the system, (b) the smaller nanocrystalline grain sizes of the components which can lead to substantial grain-size strengthening [84–86], as well as (c) the rough interlayer interfaces (as seen in the TEM images in Figs. 4–6) and incoherent interfaces that may be present within the film. Furthermore, there is no apparent thermal destabilization within the nanocomposite as there is no significant change in the hardness or reduced modulus after exposure to high

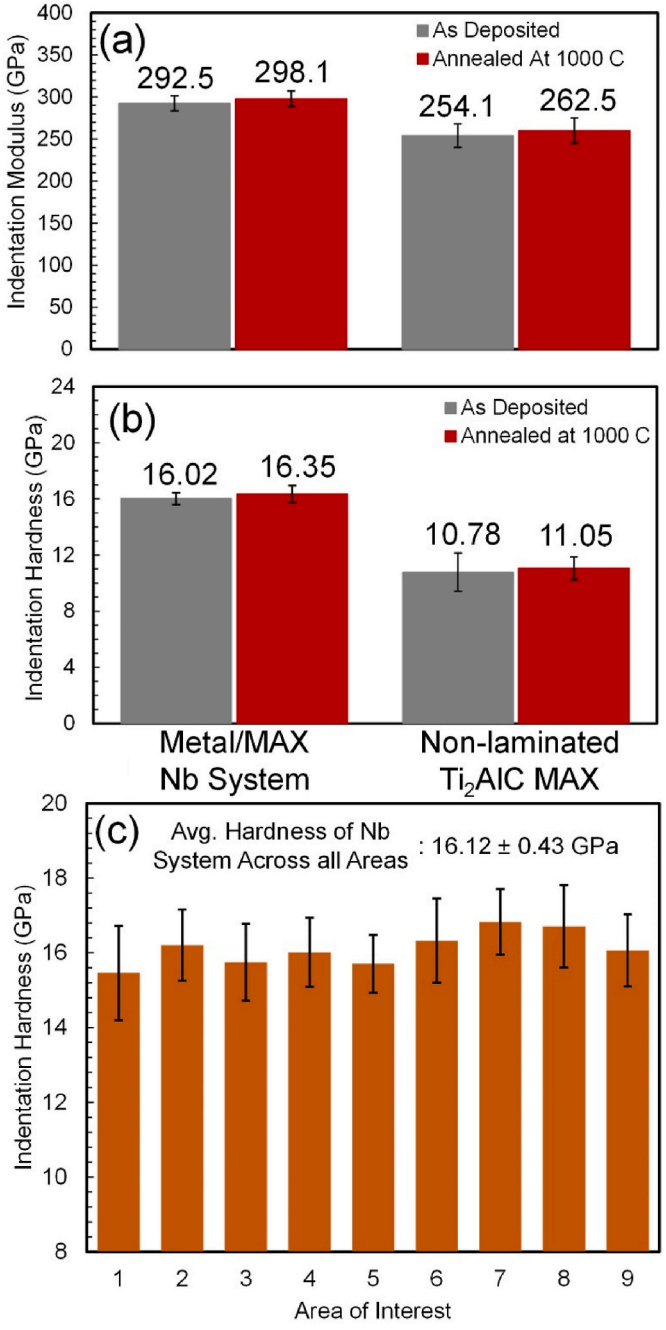

Fig. 7. (a) Indentation modulus and (b) hardness of the Nb system before and after exposure to high-temperatures of 1000 °C. All indents were performed at room temperature. (c) Indentation hardness across 9 different regions spread throughout the film surface shows the non-homogeneous nature of the deposited film.

temperatures. This thermal stability suggests that the diffusion process was mostly completed during the deposition process itself.

Fig. 8 shows engineering stress-strain curves obtained from micro-pillar compression experiments conducted on the Nb composite system; two representative tests are shown to demonstrate repeatability of the results. The relevant plastic properties, such as 0.2 % offset yield stress, and stress at instability in these pillars are summarized in the table in Fig. 8 (inset). The Nb system demonstrates a high yield stress of 4.88 ± 0.1 GPa, which is several times higher than values reported for TiC_x and TiC composites (0.15–2.27 GPa) [87–89]. The material hardens slightly after yielding to an instability stress of 5.57 ± 0.03 GPa over a strain of

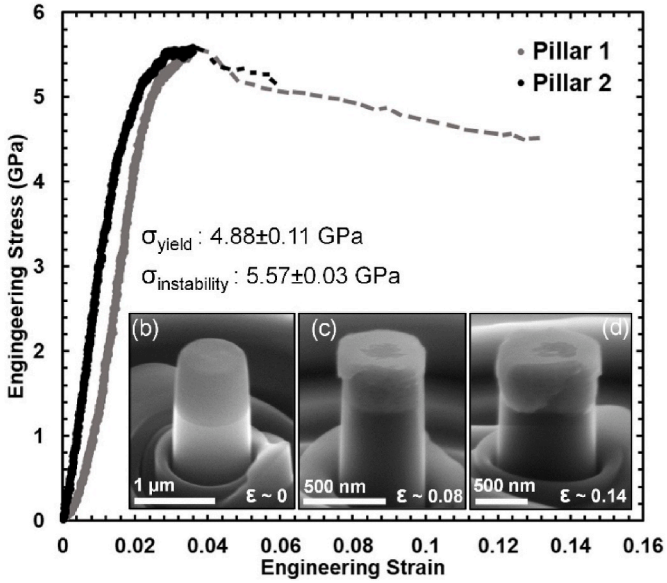

Fig. 8. Two representative engineering stress – strain responses from micro-pillar compression experiments on the Nb system. *Inset:* a table of the 0.2 % yield stress and instability stress. *Inset bottom.* Snapshots of the micropillar deformation captured before, during, and after the compression tests. The tests show consistency with the yield stress being within expectations of a rule – of – mixtures approximation (considering Hall Petch strengthening mechanisms).

~1 %. The engineering stress-strain curves after the instability point are marked by dotted lines indicating that the stress state is no longer uniaxial, and hence no quantitative analysis is possible beyond this point. SEM images of the micro-pillars taken at strains of 0, ~0.08, and ~0.15 are shown in Fig. 8b, c and d, respectively. Slip across the layers appears to be the main mode of deformation with slip being impeded by the nanolaminate layers as observed by the step-like slip trace seen in the snapshots at 0.08 and 0.14 strains.

3.4. *Ti system: microstructural, nanoindentation, and micropillar compression*

The Ti system was deposited with a similar procedure using alternating layers of Ti and Ti_2AlC at 900 °C (Fig. 9a). Fig. 9b shows the background subtracted GI-XRD profiles from the Ti system showing distinct substrate peaks that can be identified and indexed with GI-XRD. Distinct peaks for MAX phase Ti_2AlC are observed at 36.3°, 39.7°, and 62°, as well as a possible peak for Ti_3AlC_2 at 73°. There is also a single peak for Ti at 38.35° which suggests that the presence of elemental Ti in the system. Other noticeable peaks at 40.75° and 42.1° correspond the closest to Ti_3Al and $TiAl_3$ respectively, suggesting that Ti–Al intermetallics are also present. As observed in the Nb system, diffusion is possible due to the high temperature of the deposition process, which can lead to the formation of Ti–Al intermetallics. Presence of Ti_3Al, TiAl, and $TiAl_3$ intermetallics have also been reported in literature during the deposition of Ti_2AlC MAX phase [91].

Brightfield TEM micrograph (Fig. 10a) of the as-deposited Ti system thin film reveals a loss in layers despite the layered deposition. SAED (Fig. 10b) of the yellow encircled region shows randomly distributed diffractions spots signifying a randomly oriented polycrystalline film. Indexing of the polycrystalline rings in the SAED match with both Ti_2AlC and Ti_3AlC_2 phases of MAX phase with families of $\{10\bar{1}4\}$, $\{20\bar{2}3\}$ and $\{10\bar{1}1\}$, $\{10\bar{1}2\}$, $\{20\bar{2}6\}$, respectively. Tilting the specimen to the diffraction spot indexed to correspond to Ti_2AlC {0004} (highlighted in the red circle) and taking a dark field TEM micrograph (Fig. 10c) with respect to this plane illuminates the corresponding grains. From Fig. 10c, the grain size distribution for grains of Ti_2AlC {0004}

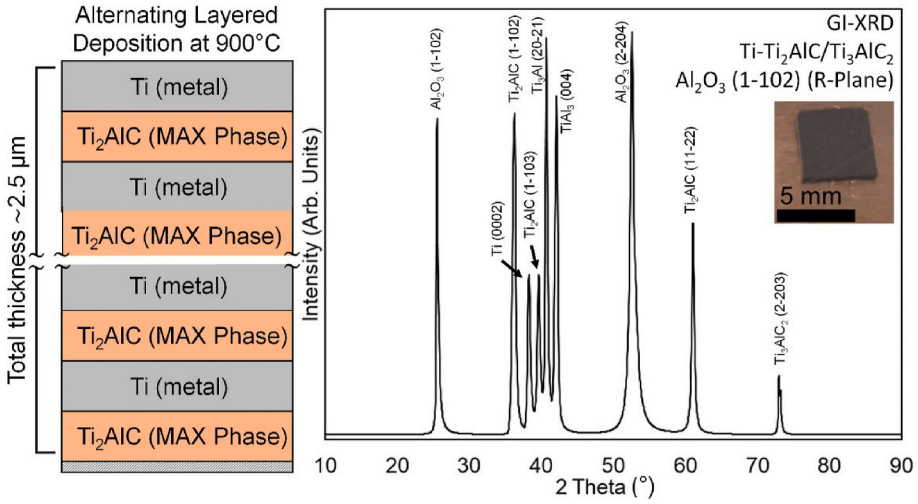

Fig. 9. (left) Schematic of the (targeted) layered deposition of the Ti system from elemental Ti, Al, and C targets. (right) GI-XRD of the deposited film on top of Al_2O_3 (10 $\bar{1}$ 2) substrate. The presence of Ti and $Ti_{n+1}AlC_n$ suggests a promising deposition on the Al_2O_3 (10 $\bar{1}$ 2) substrate, though there is also the presence of Ti–Al intermetallic phases as well.

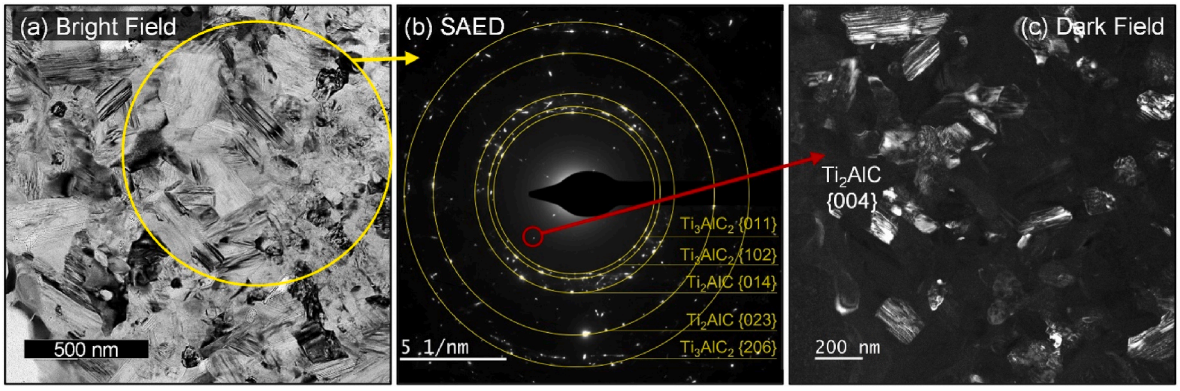

Fig. 10. Brightfield TEM micrograph (a) of the Ti/Ti_2AlC alternating deposition at 900 °C. SAED (b) of the yellow encircled region shows randomly distributed diffractions spots signifying a randomly oriented polycrystalline film. Tilting the specimen to the diffraction spot indexed to correspond to Ti_2AlC {0004} (highlighted in the red circle) and taking a dark field TEM micrograph (c) with respect to this plane illuminates the corresponding grains. (For interpretation of the references to colour in this figure legend, the reader is referred to the Web version of this article.)

orientation within this local region shows a large spread of 83.2 ± 50.6 nm.

Berkovich indentation measurements on the Ti system reveal an indentation modulus of 214.8 ± 9.8 GPa and an indentation hardness of 11.1 ± 1.2 GPa (Fig. 11a). These values are lower compared to the reported values in literature for the 211 and 312 $Ti_{n+1}AlC_n$ (n = 1,2) MAX phases (modulus ~ 277–297 GPa, hardness ~ 13.5–17.5 GPa, see Table S1 [45,92,111]). Furthermore, micro-pillar compression experiments on the Ti system show brittle fracture and catastrophic failure at an instability stress of (6.21 ± 0.25 GPa) shortly after reaching yield stress (5.61 ± 0.28 GPa) (see Fig. 11b and Supplementary video V1). Post deformed images of the micropillars taken to a stress level prior to complete failure reveal crack propagation from the top surface of the micropillar, down the side of the micropillar following a jagged columnar grain boundary (Fig. 11b, inset).

4. Discussion

4.1. Partially diffused layered microstructure of the Nb system

With the diffusion that has occurred between the layers – likely due to the elevated temperatures during the deposition process – it is challenging to identify the phases present and their volume fraction within the film of the Nb system. Multiple phases are observed in the XRD pattern in Fig. 3, however without introducing a standard reference into the deposition, it is difficult to extrapolate the phase fractions from the XRD peaks. Furthermore, from the SAED taken from the overall film in Fig. 4, the randomly distributed diffraction spots make it difficult to try to confirm the phases present in the sample. There is no particular texture observed nor phase that can be particularly identified from the SAED pattern. From the EDS line scan in Fig. 5, we can get an idea of the distribution of the elements along the line profile; however, it is difficult to confidently use this to identify the various phases and their volume fraction present in the film. Similarly, while we can get an idea of what some expected phases may be present in the film from the XRD (Fig. 3), it is challenging to quantify the volume fraction of the phases without using a technique such as precession electron diffraction. Through the HR-TEM micrographs (Fig. 6), we can identify some of the phases present and get an estimate of their volume fraction in the local region, however these are very local investigations which may not accurately represent the entirety of the film.

From the STEM investigations (Fig. 5), we observed a lower number of counts of Al in what was expected to be the MAX phase layers as compared to the expected Nb layer. A possible explanation is that Al has diffused through the system at these elevated deposition temperatures (900 °C), which can be explained if we consider the properties of Al and

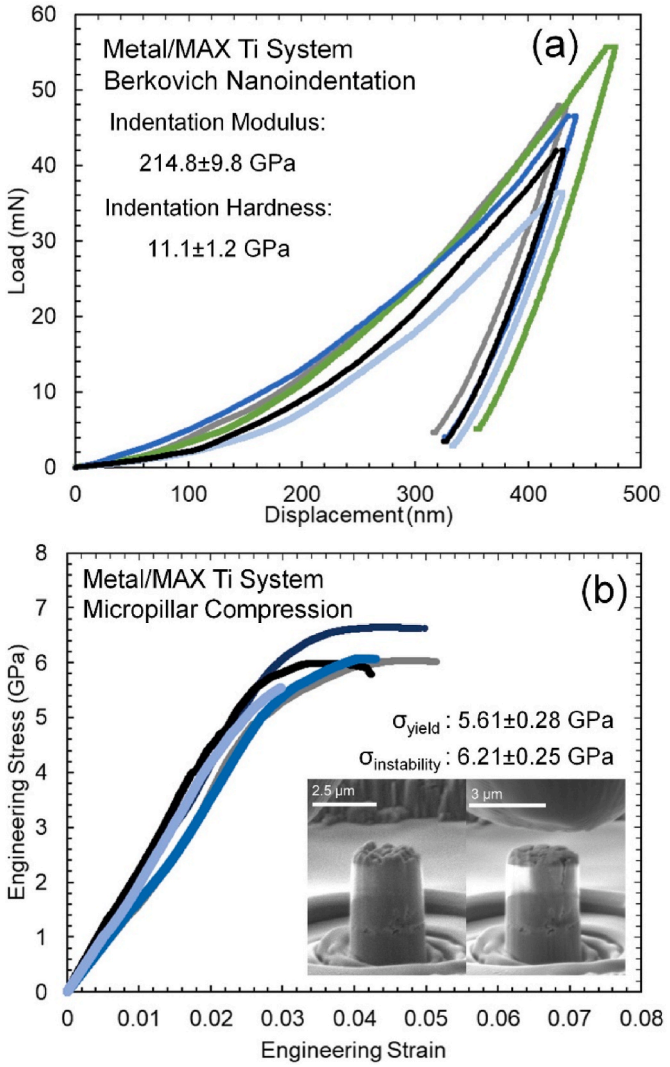

Fig. 11. (a) Representative nanoindentation load-displacement responses of the Ti system. Inset table shows measured values of modulus and hardness from the nanoindentation measurements. **(b) Representative e**ngineering stress-strain responses of the Ti system from micro-pillar compression tests. Four representative tests, one stopped at a lower strain level and others at higher strain levels, are shown in order to demonstrate the repeatability of the results. *Insets* show a table of the calculated 0.2 % yield stress and instability stress values, and snapshots of the micropillar deformation before and after compression to engineering **s**train of ~0.03, prior to catastrophic failure.

its bonding between the atoms in the Ti_2AlC MAX phase. It is known that in the 211 MAX phase family the 'A' layer element (in our case Al in Ti_2AlC) has a metallic bond with the layer of 'M' element and an ionic bond with the 'X' element [40,67]. In addition, the 'M' and 'X' element are directionally covalently bonded in an octahedral connected at the octahedra edges to form a layer with other MX octahedra. The 'A' element layer resides in between the layers of MX octahedra. In the Ti_2AlC MAX phase, the 'A' component is Al and TiC is the MX octahedra. We hypothesize that the low melting point of Al (~660 °C) and the weak bond between Ti–Al (compared to the mixed covalent–ionic–metallic bond of TiC [68]) allowed for the diffusion and movement of Al between the TiC grain boundaries. This Al diffusion out of the MAX phase in our system may be similar to the leeching of Al to form MXene using hydrofluoric acid [69–71]. Moreover, similar phase separation of Al from the MAX phase has also been reported in literature at high temperatures above 1300 °C and high pressures above 3 GPa [72,73]. We suspect the high temperature associated with the Nb deposition is likely the main culprit in allowing the movement of Al atoms. And thus, instead of the expected Nb/Ti_2AlC nanolaminate, the system stabilizes in the intermetallic phases of Nb and Al at these elevated temperatures. Such intermetallics have been shown to generally possess good oxidation resistance, high melting points, and relatively high hardness [74] compared to their individual components, although with limited strength and toughness over a wide range of temperatures [75–79].

In summary, the TEM results indicate that the as-deposited nanolaminate consists of various phases such as Ti_2AlC and Nb_2AlC MAX phases, TiC and an intermetallic Nb_xAl_y compound. The lamellar architecture was observed to have varying thicknesses. The Nb-rich regions (estimated average thickness of 32.2 ± 0.7 nm) was found to consist of both the Nb_2AlC and Nb_xAl_y phases, and the Ti-rich regions (estimated average thickness of 29.5 ± 0.8 nm) was found to consist of both the Ti_2AlC and TiC phases. The XRD results mentioned earlier in Fig. 3 are consistent with these observations.

4.2. Micro-mechanical properties of the Nb system

Table S1 compares the mechanical properties observed in the Nb system to the reported literature values of Ti_2AlC, TiC, Nb_xAl_y, and Nb_2AlC synthesized by various techniques from indentation and compression measurements [83,90–107]. From this table, the upper and lower bounds (isostress and isostrain values) of modulus and hardness of the Nb system are estimated to 293.3 GPa and 288.7 GPa for modulus [90,95,98,99,102] and 16.71 to 14.04 GPa for hardness respectively (for more details on this approximation, see the supplementary information). Our measured values of modulus (292.5 ± 8.9 GPa) and hardness (16.02 ± 0.42 GPa) for the Nb system fall within these ranges. Interestingly the yield strength of the Nb system (4.88 ± 0.1 GPa) is significantly higher than the reported values in literature for any of its individual component parts. For example, TiC_x and TiC composites have been reported to have yield strengths varying from 0.15 to 2.27 GPa [87–89] and Nb_xAl_y alloys and composites exhibit yield stresses as high as 1.01 GPa [90,94,103] (see Table S1). This discrepancy in the yield strength values may be related to differences in the measured and actual volume fraction of phases present in the sample especially considering the heterogeneity of the deposition observed in Fig. 7c. As observed in the TEM investigations and SAD pattern in Figs. 4 and 6, there is a high probability of multiple phases and grains present in the layers. Another possibility is the difference in grain size reported in literature versus the Nb system. Most of the grain sizes reported in Table S1 are in the μm range, whereas the Nb system shown in Figs. 3–8 possess grain sizes ranging from 29.5 to 32.2 nm (single grain through the layer thickness). Thus, a combination of grain size strengthening (expected yield strength and hardness are 4.82 GPa and 6.76 GPa, respectively), and confined layer slip (expected yield strength are 2.07 GPa and 6.2 GPa, respectively) may explain the enhanced yield strength and hardness of the Nb system.

4.3. Loss in layered microstructure in the Ti system

As observed in the BF-TEM of the microstructure (Fig. 10a), we speculate that, similar to the Nb system, diffusion has led to the degradation of the multilayered architecture and a complete loss of layering in the Ti system. However, for the Nb system, there is an immiscibility between Nb and Ti which serves to allow the system to retain some layered distinction. With the Ti system, there is no such immiscibility, so the species are able to diffuse extensively throughout the layers. The metal Ti layer essentially functions as excess Ti in the system at the high deposition temperatures of 800 °C – which is 0.48 T_m of Ti and 1.26 T_m of Al – resulting in the formation of binary phases of Ti–Al (i.e. Ti_3Al and $TiAl_3$) and ternary phases of Ti–Al–C (Ti_2AlC and Ti_3AlC_2) as seen in both the GI-XRD profiles (Fig. 9) and the SAED rings (Fig. 10).

As mentioned earlier, PVD deposition of MAX phases requires high deposition temperatures (>700 °C), especially if the goal is to obtain

textured epitaxial growth. Unlike multilayered nanocomposites deposited at room temperatures, especially immiscible systems such as Ag/Ni, Cu/TiN, and Mg/Nb multilayers [31,108,109], such high temperatures can result in significant diffusion within the metal/MAX nanolaminate structure. For example, in the Nb/Ti_2AlC metal/MAX system (Fig. 1c, [4–6]) these higher temperatures are speculated to have caused Al (melting point of ~660 °C) to become mobile and diffuse through the system, potentially diffusing out of the MAX phase system [72,73]. As shown in Figs. 4–6, this diffusion leads to the formation of unexpected phases (impurities) in the layered system, such as Nb_xAl_y intermetallic, $Ti_{n+1}AlC_n$ and $Nb_{n+1}AlC_n$ MAX phases, and TiC. Similarly in the Ti/Ti_2AlC metal/MAX nanolaminate, such high temperatures are speculated to cause the Ti–Al–C species in the system (Fig. 1d, 9 and 10) to stabilize in potentially a higher phase order of $Ti_{n+1}AlC_n$ (n = 2, 3 etc.) MAX phase such as the 312 system. Additionally, such diffusion in the Ti system results in a microstructure of mixed MAX phases that lack any multilayered nanolaminate architecture.

A possible alternative explanation for the loss in the layered microstructure observed after the depositions may be attributed to errors during the PVD process itself, in which certain magnetrons may have been switched on and/or off in the wrong sequence. This unlikely scenario is included only for the sake of completeness and for covering all possible explanations.

Our observations and analysis from the TEM investigations on both the Nb system and Ti system's microstructure highlight the need to effectively block/mitigate interlayer diffusion occurring at the elevated deposition temperatures of 800–900 °C in order to successfully synthesize textured epitaxial Nb,Ti/Ti_2AlC metal/MAX multilayered nanolaminates using PVD. Textured growth has been reported and reduced deposition temperatures have been observed [42–44,110], however elevated temperatures are still recommended to achieve a higher degree of epitaxy. An alternate approach for obtaining textured (nonlaminated) MAX phase Ti_2AlC and $T_{i3}AlC_2$ growth is through a two-step process; an initial step of low temperature deposition followed by post deposition heat treatment [44,92], although the success of this two-step process in depositing alternating metallic and MAX phase multilayers is yet to be explored. Diffusion is expected in the two-step deposition process as well since the heat treatment in the second step would require high temperatures above a minimum of 550 °C [42], and enhanced textured growth above ~700 °C [44].

Another strategy is to add a third layer that can act as a diffusion barrier. For example, a thin Al_2O_3 interlayer diffusion barrier deposited via atomic layer deposition (ALD) may serve as effective barrier layer, as has been reported elsewhere [12]. Alternatively, some reports also suggest the deposition of a TiC seed layer [45,111] or deposition of elemental constituents followed by post deposition heat treatment [42, 44,92] to increase the success and epitaxial growth of the MAX phase in systems involving Ti and C.

4.4. Micro-mechanical properties of the Ti system

From supplementary videos V1, this brittle failure observed is similar to what has been reported in bulk compression experiments of polycrystalline Ti_2AlC MAX phase [91,112,113]. The yield strength values of our Ti system in Fig. 11b are considerably higher than those reported for similar systems in literature for 211 as well as 312 $Ti_{n+1}AlC_n$ MAX phase [114,115] (the highest value for yield strength reported is 1.26 ± 0.05 GPa with fine grained (4.2 μm) Ti_2AlC with impurities [91]). However our values are still lower than ~9.2 GPa which would be expected from a grain size strengthened extrapolated yield strength of the Ti_2AlC system [91]. We hypothesize that the lower values may be attributed to two main factors. First, as evidenced by the XRD measurements, this system may possess trace Ti and Ti–Al intermetallic phases. It is difficult to accurately predict an expected modulus or hardness without a clear understanding of the volume fractions of the various phases. Secondly, large porosities can be seen in the micropillars (see inset SEM micrographs in Fig. 11b), which can lead to appreciable deterioration of the mechanical properties of the thin film [46,116].

5. Conclusion

In this work, we report the multilayered deposition of metal/MAX phase thin films utilizing Nb or Ti as the metal component and Ti_2AlC as the MAX phase component at elevated temperatures (900 °C and 800 °C, respectively). While the depositions were partially successful with the observation of MAX phases (as indicated by XRD and TEM), both depositions possessed unwanted microstructures that were heavily affected by diffusion due to the elevated temperatures during the deposition process, leading to a deterioration of the expected layered microstructure. In both systems, the thin films were composed of a mix of MAX phase, intermetallic, and/or carbide phases.

For the Nb system we found the following:

- Distinct layers of Nb-rich and Ti-rich regions were identified with mixed phases. We speculate that the diffusion of Al atoms from the MAX phase, driven by the high temperature depositions, led to the formation of Nb_xAl_y intermetallics, TiC, and a combination of Ti_3AlC_2 and Ti_2AlC MAX phase within the various layers.
- The indentation modulus (292.5 ± 8.9 GPa) and hardness (16.02 ± 0.42 GPa) values were within expected ranges calculated from composite theory.
- Micropillar compression experiments demonstrated a high yield strength (4.88 ± 0.1 GPa), speculated to be largely in part due to the nanocrystalline nature of the film grains leading to a grain size strengthening effect.

For the Ti system, we report the following:

- The high temperature multilayered deposition of Ti and Ti_2AlC led to a complete loss of the multilayered architecture and, rather, a mixture of binary and ternary phases of Ti–Al (Ti_3Al and $TiAl_3$) and Ti–Al–C (Ti_2AlC and Ti_3AlC_2).
- The yield (5.61 ± 0.28 GPa) and instability (6.21 ± 0.25 GPa) strengths reported here for this system are among the highest reported for similar systems in literature [91,115,117], however, they are still lower than expected from composite theory.

CRediT authorship contribution statement

Skye Supakul: Writing – review & editing, Writing – original draft, Visualization, Validation, Supervision, Methodology, Investigation, Formal analysis, Data curation, Conceptualization. **Manish Jain:** Writing – review & editing, Methodology, Investigation, Formal analysis. **Krishna Yaddanapudi:** Writing – review & editing, Writing – original draft, Investigation, Formal analysis. **Jacob Gruber:** Conceptualization. **Osman El-Atwani:** Writing – review & editing, Investigation, Formal analysis. **Garritt J. Tucker:** Writing – review & editing, Supervision, Methodology, Conceptualization. **Siddhartha Pathak:** Writing – review & editing, Writing – original draft, Visualization, Validation, Supervision, Resources, Project administration, Methodology, Funding acquisition, Data curation, Conceptualization.

Declaration of competing interest

The authors declare that they have no known competing financial interests or personal relationships that could have appeared to influence the work reported in this paper.

Data availability

Data will be made available on request.

Acknowledgements

We acknowledge funding from the Army Research Office (ARO) Proposal No. W911NF1910389 (Program manager Dan Cole), and ARO DURIP Proposal No. 77460-MS-RIP (Program manager Dan Cole) for this work. This work was performed, in part, at the Center for Integrated Nanotechnologies (CINT), an Office of Science User Facility operated for the U.S. Department of Energy (DOE) Office of Science by Los Alamos National Laboratory (Contract 89233218CNA000001) and Sandia National Laboratories (Contract DE-NA-0003525). G.J.T. is grateful for the additional support of this work by the Eula Mae and John Baugh Chair in Physics at Baylor University. Travel expenses to CINT was provided by National Science Foundation (NSF) #2051443. We thank Jon Kevin Baldwin and Sezer Picak for help with the PVD deposition and microstructural analysis. We also thank the ThinkSwiss 2022 Scholarship for providing travel support for graduate student Skye Supakul for visit to EMPA, Swiss Federal Laboratories for Materials Science and Technology in Thun, Switzerland.

Appendix A. Supplementary data

Supplementary data to this article can be found online at https://doi.org/10.1016/j.msea.2024.146905.

References

[1] P.C. Yashar, W.D. Sproul, Nanometer scale multilayered hard coatings, Vacuum 55 (3) (1999) 179–190.
[2] J.M.T. Thompson, S.J. Lloyd, J.M. Molina-Aldareguia, Multilayered materials: a palette for the materials artist, Philos. Trans. R. Soc. London, Ser. A: Math. Phys. Eng. Sci. 361 (1813) (2003) 2931–2949.
[3] X. Deng, N. Chawla, K.K. Chawla, M. Koopman, J.P. Chu, Mechanical behavior of multilayered nanoscale metal-ceramic composites, Adv. Eng. Mater. 7 (12) (2005) 1099–1108.
[4] S. Lotfian, M. Rodríguez, K.E. Yazzie, N. Chawla, J. Llorca, J.M. Molina-Aldareguía, High temperature micropillar compression of Al/SiC nanolaminates, Acta Mater. 61 (12) (2013) 4439–4451.
[5] G. Tang, Y.L. Shen, D.R.P. Singh, N. Chawla, Indentation behavior of metal–ceramic multilayers at the nanoscale: numerical analysis and experimental verification, Acta Mater. 58 (6) (2010) 2033–2044.
[6] S. Zheng, I.J. Beyerlein, J.S. Carpenter, K. Kang, J. Wang, W. Han, N.A. Mara, High-strength and thermally stable bulk nanolayered composites due to twin-induced interfaces, Nat. Commun. 4 (2013) 1696.
[7] N. Li, N.A. Mara, J. Wang, P. Dickerson, J.Y. Huang, A. Misra, Ex situ and in situ measurements of the shear strength of interfaces in metallic multilayers, Scripta Mater. 67 (5) (2012) 479–482.
[8] N.A. Mara, I.J. Beyerlein, Review: effect of bimetal interface structure on the mechanical behavior of Cu–Nb fcc–bcc nanolayered composites, J. Mater. Sci. 49 (19) (2014) 6497–6516.
[9] N.A. Mara, I.J. Beyerlein, J.S. Carpenter, J. Wang, Interfacially driven deformation twinning in bulk Ag-Cu composites, J. Occup. Med. 64 (10) (2012) 1218–1226.
[10] S.J. Zheng, I.J. Beyerlein, J. Wang, J.S. Carpenter, W.Z. Han, N.A. Mara, Deformation twinning mechanisms from bimetal interfaces as revealed by in situ straining in the TEM, Acta Mater. 60 (16) (2012) 5858–5866.
[11] Z. Czigány, G. Radnóczi, Columnar growth structure and evolution of wavy interface morphology in amorphous and polycrystalline multilayered thin films, Thin Solid Films 347 (1) (1999) 133–145.
[12] T.E.J. Edwards, T. Xie, N. Maria della Ventura, D. Casari, C. Guerra, E. Huszár, X. Maeder, J.J. Schwiedrzik, I. Utke, L. Pethö, J. Michler, On the thinnest Al2O3 interlayers in Al-based nanolaminates to enhance strength, and the role of constraint, Acta Mater. 240 (2022) 118345.
[13] B. Putz, T.E.J. Edwards, E. Huszar, L. Pethö, P. Kreiml, M.J. Cordill, D. Thiaudiere, S. Chiroli, F. Zighem, D. Faurie, P.-O. Renault, J. Michler, In situ fragmentation of Al/Al2O3 multilayers on flexible substrates in biaxial tension, Mater. Des. 232 (2023) 112081.
[14] I. Salehinia, S. Shao, J. Wang, H.M. Zbib, Plastic deformation of metal/ceramic nanolayered composites, J. Occup. Med. 66 (10) (2014) 2078–2085.
[15] T.P.D. Rajan, B.C. Pai, Developments in processing of functionally gradient metals and metal-ceramic composites: a review, Acta Metallurgica Sinica-English Letters 27 (5) (2014) 825–838.
[16] I. Knorr, N.M. Cordero, E.T. Lilleodden, C.A. Volkert, Mechanical behavior of nano scale Cu/PdSi multilayers, Acta Mater. 61 (13) (2013) 4984–4995.
[17] S. Lotfian, J.M. Molina-Aldareguia, K.E. Yazzie, J. Llorca, N. Chawla, High-temperature nanoindentation behavior of Al/SiC multilayers, Phil. Mag. Lett. 92 (8) (2012) 362–367.
[18] R. Raghavan, J.M. Wheeler, D. Esque-de los Ojos, K. Thomas, E. Almandoz, G. G. Fuentes, J. Michler, Mechanical behavior of Cu/TiN multilayers at ambient and elevated temperatures: stress-assisted diffusion of Cu, Mater. Sci. Eng. a-Struct. Mater. Propert. Microstruct. Proc. 620 (2015) 375–382.
[19] N. Mara, I. Beyerlein, Review: effect of bimetal interface structure on the mechanical behavior of Cu–Nb fcc–bcc nanolayered composites, J. Mater. Sci. 49 (19) (2014) 6497–6516.
[20] I.J. Beyerlein, N.A. Mara, J.S. Carpenter, T. Nizolek, W.M. Mook, T.A. Wynn, R. J. McCabe, J.R. Mayeur, K. Kang, S. Zheng, J. Wang, T.M. Pollock, Interface-driven microstructure development and ultra high strength of bulk nanostructured Cu-Nb multilayers fabricated by severe plastic deformation, J. Mater. Res. 28 (13) (2013) 1799–1812.
[21] S. Pathak, N. Velisavljevic, J.K. Baldwin, M. Jain, S. Zheng, N.A. Mara, I. J. Beyerlein, Strong, ductile, and thermally stable bcc-Mg nanolaminates, Sci. Rep. 7 (1) (2017) 8264.
[22] I. Knorr, N.M. Cordero, E.T. Lilleodden, C.A. Volkert, Mechanical behavior of nanoscale Cu/PdSi multilayers, Acta Mater. 61 (13) (2013) 4984–4995.
[23] R. Raghavan, J.M. Wheeler, D. Esqué-de los Ojos, K. Thomas, E. Almandoz, G. G. Fuentes, J. Michler, Mechanical behavior of Cu/TiN multilayers at ambient and elevated temperatures: stress-assisted diffusion of Cu, Mater. Sci. Eng., A 620 (2015) 375–382.
[24] S. Lotfian, C. Mayer, N. Chawla, J. Llorca, A. Misra, J.K. Baldwin, J.M. Molina-Aldareguía, Effect of layer thickness on the high temperature mechanical properties of Al/SiC nanolaminates, Thin Solid Films 571 (2014) 260–267.
[25] D.R.P. Singh, N. Chawla, G. Tang, Y.L. Shen, Micropillar compression of Al/SiC nanolaminates, Acta Mater. 58 (20) (2010) 6628–6636.
[26] S. Lotfian, C. Mayer, N. Chawla, J. Llorca, A. Misra, J.K. Baldwin, J.M. Molina-Aldareguía, Effect of layer thickness on the high temperature mechanical properties of Al/SiC nanolaminates, Thin Solid Films 571 (Part 2) (2014) 260–267.
[27] W.M. Mook, R. Raghavan, J.K. Baldwin, D. Frey, J. Michler, N.A. Mara, A. Misra, Indentation fracture response of Al–TiN nanolaminates, Mater. Res. Lett. 1 (2) (2013) 102–108.
[28] D. Bhattacharyya, N.A. Mara, P. Dickerson, R.G. Hoagland, A. Misra, A transmission electron microscopy study of the deformation behavior underneath nanoindents in nanoscale Al-TiN multilayered composites, Phil. Mag. 90 (13) (2010) 1711–1724.
[29] D. Bhattacharyya, N.A. Mara, P. Dickerson, R.G. Hoagland, A. Misra, Compressive flow behavior of Al-TiN multilayers at nanometer scale layer thickness, Acta Mater. 59 (10) (2011) 3804–3816.
[30] D. Bhattacharyya, N.A. Mara, R.G. Hoagland, A. Misra, Nanoindentation and microstructural studies of Al/TiN multilayers with unequal volume fractions, Scripta Mater. 58 (11) (2008) 981–984.
[31] S. Pathak, N. Li, X. Maeder, R.G. Hoagland, J.K. Baldwin, J. Michler, A. Misra, J. Wang, N.A. Mara, On the origins of hardness of Cu–TiN nanolayered composites, Scripta Mater. 109 (2015) 48–51.
[32] J. Wang, A. Misra, Strain hardening in nanolayered thin films, Curr. Opin. Solid State Mater. Sci. 18 (1) (2014) 19–28.
[33] N. Li, H. Wang, A. Misra, J. Wang, In situ nanoindentation study of plastic Co-deformation in Al-TiN nanocomposites, Sci. Rep. 4 (2014).
[34] M.W. Barsoum, The MN+1AXN phases: a new class of solids: thermodynamically stable nanolaminates, Prog. Solid State Chem. 28 (1–4) (2000) 201–281.
[35] M.W. Barsoum, T. El-Raghy, The MAX phases: unique new carbide and nitride materials, Am. Sci. 89 (4) (2001) 334.
[36] P. Eklund, M. Beckers, U. Jansson, H. Högberg, L. Hultman, The Mn + 1AXn phases: materials science and thin-film processing, Thin Solid Films 518 (8) (2010) 1851–1878.
[37] M.W. Barsoum, M. Radovic, Elastic and mechanical properties of the MAX phases, Annu. Rev. Mater. Res. 41 (1) (2011) 195–227.
[38] J. Gruber, A.C. Lang, J. Griggs, M.L. Taheri, G.J. Tucker, M.W. Barsoum, Evidence for bulk ripplocations in layered solids, Sci. Rep. 6 (2016) 33451.
[39] M. Sundberg, G. Malmqvist, A. Magnusson, T. El-Raghy, Alumina forming high temperature silicides and carbides, Ceram. Int. 30 (7) (2004) 1899–1904.
[40] M.W. Barsoum, M. Radovic, Elastic and mechanical properties of the MAX phases, Annu. Rev. Mater. Res. 41 (1) (2011) 195–227.
[41] D.J. Tallman, L. He, B.L. Garcia-Diaz, E.N. Hoffman, G. Kohse, R.L. Sindelar, M. W. Barsoum, Effect of neutron irradiation on defect evolution in Ti3SiC2 and Ti2AlC, J. Nucl. Mater. 468 (2016) 194–206.
[42] Z. Wang, W. Li, Y. Liu, J. Shuai, P. Ke, A. Wang, Diffusion-controlled intercalation approach to synthesize the Ti2AlC MAX phase coatings at low temperature of 550 °C, Appl. Surf. Sci. 502 (2020) 144130.
[43] Z. Wang, W. Li, C. Wang, H. Wu, P. Ke, A. Wang, Transforming the amorphous Ti-Al-C coatings to high-purity Ti2AlC MAX phase coatings by prolonged annealing at 550 °C, Mater. Lett. 261 (2020) 127160.
[44] C. Tang, M. Steinbrück, M. Klimenkov, U. Jäntsch, H.J. Seifert, S. Ulrich, M. Stüber, Textured growth of polycrystalline MAX phase carbide coatings via thermal annealing of M/C/Al multilayers, J. Vac. Sci. Technol. A 38 (1) (2019) 013401.
[45] O. Wilhelmsson, J.P. Palmquist, T. Nyberg, U. Jansson, Deposition of Ti2AlC and Ti3AlC2 epitaxial films by magnetron sputtering, Appl. Phys. Lett. 85 (6) (2004) 1066–1068.
[46] J. Frodelius, Thick and Thin Ti2AlC Coatings, Linköping Studies in Science and Technology, Dissertations, Linköping University Electronic Press, Linköping, 2010, p. 63.
[47] P. Eklund, M. Beckers, U. Jansson, H. Högberg, L. Hultman, The Mn+1AXn phases: materials science and thin-film processing, Thin Solid Films 518 (8) (2010) 1851–1878.

[48] R. Su, H. Zhang, D.J. O'Connor, L. Shi, X. Meng, H. Zhang, Deposition and characterization of Ti2AlC MAX phase and Ti3AlC thin films by magnetron sputtering, Mater. Lett. 179 (2016) 194–197.
[49] J. Frodelius, P. Eklund, M. Beckers, P.O.Å. Persson, H. Högberg, L. Hultman, Sputter deposition from a Ti2AlC target: process characterization and conditions for growth of Ti2AlC, Thin Solid Films 518 (6) (2010) 1621–1626.
[50] W. Garkas, C. Leyens, A. Flores-Renteria, Synthesis and characterization of Ti2AlC and Ti2AlN MAX phase coatings manufactured in an industrial-size coater, Adv. Mater. Res. 89–91 (2010) 208–213.
[51] J. Emmerlich, H. Högberg, S. Sasvári, P. Persson, L. Hultman, J.-P. Palmquist, U. Jansson, J.M. Molina-Aldareguia, Z. Czigány, Growth of Ti3SiC2 thin films by elemental target magnetron sputtering, J. Appl. Phys. 96 (9) (2004) 4817–4826.
[52] S. Pathak, S.R. Kalidindi, Spherical nanoindentation stress–strain curves, Mater. Sci. Eng. R Rep. 91 (2015) 1–36.
[53] W.C. Oliver, G.M. Pharr, Measurement of hardness and elastic modulus by instrumented indentation: advances in understanding and refinements to methodology, J. Mater. Res. 19 (1) (2004) 3–20.
[54] W.C. Oliver, G.M. Pharr, An improved technique for determining hardness and elastic modulus using load and displacement sensing indentation experiments, J. Mater. Res. 7 (6) (1992) 1564–1583.
[55] G.M. Pharr, J.H. Strader, W.C. Oliver, Critical issues in making small-depth mechanical property measurements by nanoindentation with continuous stiffness measurement, J. Mater. Res. 24 (3) (2009) 653–666.
[56] J. Wang, C. Yang, P.D. Hodgson, Strain gradients in Cu–Fe thin films and multilayers during micropillar compression, Mater. Sci. Eng., A 651 (2016) 146–154.
[57] D. Raabe, D. Ma, F. Roters, Effects of initial orientation, sample geometry and friction on anisotropy and crystallographic orientation changes in single crystal microcompression deformation: a crystal plasticity finite element study, Acta Mater. 55 (13) (2007) 4567–4583.
[58] A. Kunz, S. Pathak, J.R. Greer, Size effects in Al nanopillars: single crystalline vs. bicrystalline, Acta Mater. 59 (11) (2011) 4416–4424.
[59] D. Kiener, C. Motz, G. Dehm, Micro-compression testing: a critical discussion of experimental constraints, Mater. Sci. Eng., A 505 (1) (2009) 79–87.
[60] M. Ardeljan, M. Knezevic, M. Jain, S. Pathak, A. Kumar, N. Li, N.A. Mara, J. K. Baldwin, I.J. Beyerlein, Room temperature deformation mechanisms of Mg/Nb nanolayered composites, J. Mater. Res. 33 (10) (2018) 1311–1332.
[61] C. Wang, T. Yang, J. Xiao, S. Liu, J. Xue, J. Wang, Q. Huang, Y. Wang, Irradiation-induced structural transitions in Ti2AlC, Acta Mater. 98 (2015) 197–205.
[62] Z.J. Lin, M.J. Zhuo, Y.C. Zhou, M.S. Li, J.Y. Wang, Microstructural characterization of layered ternary Ti2AlC, Acta Mater. 54 (4) (2006) 1009–1015.
[63] Z. Liu, Y. Chen, L. Du, P. Li, Y. Cui, X. Pan, G. Yan, Preparation of Nb3Al superconductor by powder metallurgy and effect of mechanical alloying on the phase formation, J. Modern Transport. 22 (1) (2014) 55–58.
[64] T.S. Kumar, S.R. Kumar, M.L. Rao, T.L. Prakash, Preparation of niobium metal powder by two-stage magnesium vapor reduction of niobium pentoxide, J. Metall. 2013 (2013) 1–6.
[65] R. Olivares-Navarrete, J. Olaya, C. Ramírez, S. Rodil, Biocompatibility of niobium coatings, Coatings 1 (2011) 72–87.
[66] P. Mondal, M. Manekar, R. Kumar, T. Ganguli, S.B. Roy, Superconducting properties of nanocrystalline Nb3Al in Nb–Al matrix, Appl. Phys. Lett. 92 (5) (2008) 052507.
[67] M.W. Barsoum, MAX Phases: Properties of Machinable Ternary Carbides and Nitrides, 2013. Wiley.
[68] N.I. Medvedeva, D.L. Novikov, A.L. Ivanovsky, M.V. Kuznetsov, A.J. Freeman, Electronic properties of ${\mathrm{Ti}}_{3}{\mathrm{SiC}}_{2}$-based solid solutions, Phys. Rev. B 58 (24) (1998) 16042–16050.
[69] R. Syamsai, P. Kollu, S. Kwan Jeong, A. Nirmala Grace, Synthesis and properties of 2D-titanium carbide MXene sheets towards electrochemical energy storage applications, Ceram. Int. 43 (16) (2017) 13119–13126.
[70] W. Sun, S.A. Shah, Y. Chen, Z. Tan, H. Gao, T. Habib, M. Radovic, M.J. Green, Electrochemical etching of Ti2AlC to Ti2CTx (MXene) in low-concentration hydrochloric acid solution, J. Mater. Chem. A 5 (41) (2017) 21663–21668.
[71] M. Naguib, J. Come, B. Dyatkin, V. Presser, P.-L. Taberna, P. Simon, M. W. Barsoum, Y. Gogotsi, MXene: a promising transition metal carbide anode for lithium-ion batteries, Electrochem. Commun. 16 (1) (2012) 61–64.
[72] J. Qin, D. He, C. Chen, J. Wang, J. Hu, B. Yang, Phase segregation of titanium-aluminium carbide (Ti2AlC) at high pressure and high temperature, J. Alloys Compd. 462 (1) (2008) L24–L27.
[73] X.H. Wang, Y.C. Zhou, High-temperature oxidation behavior of Ti2AlC in air, Oxid. Metals 59 (3) (2003) 303–320.
[74] C.T. Liu, Recent advances in ordered intermetallics, Mater. Chem. Phys. 42 (2) (1995) 77–86.
[75] T.W.B. Riyadi, M. Mujiyono, D. Nurhadiyanto, A.F.H. Mukhammad, S.B. A. Hassan, A.P. Wulandari, M. Murni, Fabrication of NiAl and TiC intermetallic matrix composite coatings, Compos. Interfac. (2021) 1–16.
[76] X. Fan, W. Huang, X. Zhou, B. Zou, Preparation and characterization of NiAl–TiC–TiB2 intermetallic matrix composite coatings by atmospheric plasma spraying of SHS powders, Ceram. Int. 46 (8, Part A) (2020) 10512–10520.
[77] Y. Lu, M. Watanabe, R. Miyata, J. Nakamura, J. Yamada, H. Kato, K. Yoshimi, Microstructures and mechanical properties of TiC-particulate-reinforced Ti–Mo–Al intermetallic matrix composites, Mater. Sci. Eng., A 790 (2020) 139523.
[78] R. Chen, Y. Tan, H. Fang, L. Luo, H. Ding, Y. Su, J. Guo, H. Fu, Macro/microstructure evolution and mechanical properties of Ti33.3Al alloys by adding WC particles, Mater. Sci. Eng., A 725 (2018) 171–180.
[79] W. Liu, J.N. DuPont, Fabrication of carbide-particle-reinforced titanium aluminide-matrix composites by laser-engineered net shaping, Metall. Mater. Trans. 35 (13) (2004) 1133–1140.
[80] J. Singh, M.F. Wani, S. Banday, C. Shekhar, G. Singh, Nano scratch and nanoindentation: an approach to understand the tribological behaviour of max phase material Ti2AlC, IOP Conf. Ser. Mater. Sci. Eng. 561 (2019) 012111.
[81] S. Liu, C. Wang, T. Yang, Y. Fang, Q. Huang, Y. Wang, High temperature effects on irradiation damage of Ti2AlC, Nucl. Instrum. Methods Phys. Res. Sect. B Beam Interact. Mater. Atoms 406 (2017) 662–669.
[82] J. Wang, W.-Z. Li, H.-D. Li, B. Shi, J.-B. Luo, Nanoindentation study on the mechanical properties of Tic/Mo multilayers, Thin Solid Films 366 (1) (2000) 117–120.
[83] R.W. Rice, C.C. Wu, F. Boichelt, Hardness–grain-size relations in ceramics, J. Am. Ceram. Soc. 77 (10) (1994) 2539–2553.
[84] N. Hansen, Hall–Petch relation and boundary strengthening, Scripta Mater. 51 (8) (2004) 801–806.
[85] N.J. Petch, The cleavage strength of polycrystals, J. Iron Steel Inst. 174 (1953) 25–28.
[86] E.O. Hall, The deformation and ageing of mild steel: III Discussion of results, Proc. Phys. Soc. B 64 (9) (1951) 747–753.
[87] C.Y. Tang, C.T. Wong, L.N. Zhang, M.T. Choy, T.W. Chow, K.C. Chan, T.M. Yue, Q. Chen, In situ formation of Ti alloy/TiC porous composites by rapid microwave sintering of Ti6Al4V/MWCNTs powder, J. Alloys Compd. 557 (2013) 67–72.
[88] A.R. Kennedy, S.M. Wyatt, Characterising particle–matrix interfacial bonding in particulate Al–TiC MMCs produced by different methods, Compos. Appl. Sci. Manuf. 32 (3) (2001) 555–559.
[89] G. Das, K.S. Mazdiyasni, H.A. Lipsitt, Mechanical properties of polycrystalline TiC, J. Am. Ceram. Soc. 65 (2) (1982) 104–110.
[90] H.M. Enginsoy, F. Gatamorta, E. Bayraktar, M.H. Robert, I. Miskioglu, Experimental and numerical study of Al-Nb2Al composites via associated procedure of powder metallurgy and thixoforming, Compos. B Eng. 162 (2019) 397–410.
[91] R. Benitez, H. Gao, M. O'Neal, P. Lovelace, G. Proust, M. Radovic, Effects of microstructure on the mechanical properties of Ti2AlC in compression, Acta Mater. 143 (2018) 130–140.
[92] C. Tang, M. Klimenkov, U. Jaentsch, H. Leiste, M. Rinke, S. Ulrich, M. Steinbrück, H.J. Seifert, M. Stueber, Synthesis and characterization of Ti2AlC coatings by magnetron sputtering from three elemental targets and ex-situ annealing, Surf. Coating. Technol. 309 (2017) 445–455.
[93] M. Aybey, T. Yener, M. Ipek, S. Zeytin, Effect of holding time on the production of Nb-NbAl3 intermetallic composites via electric-Current-activated sintering, Materiali in tehnologije 51 (2017) 55–58.
[94] G.E. Bean, F. Ebrahimi, M.V. Manuel, High temperature deformation of Ti–Al–Nb–Cr–Mo alloy with ultrafine microstructure, Intermetallics 49 (2014) 132–137.
[95] A. Nino, A. Tanaka, S. Sugiyama, H. Taimatsu, Indentation size effect for the hardness of refractory carbides, Mater. Trans. 51 (9) (2010) 1621–1626.
[96] J. Musil, P. Novák, R. Čerstvý, Z. Soukup, Tribological and mechanical properties of nanocrystalline-TiC/a-C nanocomposite thin films, J. Vac. Sci. Technol. A 28 (2) (2010) 244–249.
[97] C.T. Rios, A.A. Coelho, W.W. Batista, M.C. Gonçalves, R. Caram, ISE and fracture toughness evaluation by Vickers hardness testing of an Al3Nb–Nb2Al–AlNbNi in situ composite, J. Alloys Compd. 472 (1) (2009) 65–70.
[98] F. Sergejev, M. Antonov, Comparative study on indentation fracture toughness measurements of cemented carbides/Kermiste purunemissitkuse maaramise indenteerimismeetodite vordlev analuus, Proc. Est. Acad. Sci. Eng. 12 (2006) 388 +.
[99] C. Triveño Rios, P. Ferrandini, R. Caram, Fracture toughness of the eutectic alloy Al3Nb-Nb2Al, Mater. Lett. 57 (24) (2003) 3949–3953.
[100] I. Salama, T. El-Raghy, M.W. Barsoum, Synthesis and mechanical properties of Nb2AlC and (Ti,Nb)2AlC, J. Alloys Compd. 347 (1) (2002) 271–278.
[101] V. Gauthier, F. Bernard, E. Gaffet, Z.A. Munir, J.P. Larpin, Synthesis of nanocrystalline NbAl3 by mechanical and field activation, Intermetallics 9 (7) (2001) 571–580.
[102] J. Wang, W.-Z. Li, H.-D. Li, B. Shi, J.-B. Luo, Nano-indentation study on the mechanical properties of TiC/Mo multilayers deposited by ion beam assisted deposition, Surf. Coating. Technol. 128–129 (2000) 161–165.
[103] T. Kumagai, S. Hanada, Microstructure of Nb2Al-NbAl3 eutectic alloys produced by unidirectional solidification, Mater. Sci. Eng., A 152 (1) (1992) 349–355.
[104] E.P. Barth, J.K. Tien, S. Uejo, S. Kambara, High temperature strength of niobium aluminide intermetallics, Mater. Sci. Eng., A 153 (1) (1992) 398–401.
[105] S. Tsurekawa, S. Matsubara, H. Kurishita, H. Yoshinaga, Steady state deformation mechanism in titanium carbide, Mater. Trans. JIM 32 (9) (1991) 821–828.
[106] D.B. Miracle, H.A. Lipsitt, Mechanical properties of fine-grained substoichiomebic titanium carbide, J. Am. Ceram. Soc. 66 (8) (1983) 592–597.
[107] G.E. Hollox, R.E. Smallman, Plastic behavior of titanium carbide, J. Appl. Phys. 37 (2) (1966) 818–823.
[108] M. Jain, N. Velisavljevic, J.K. Baldwin, M. Knezevic, N.A. Mara, I.J. Beyerlein, S. Pathak, Structure and properties of pseudomorphically transformed bcc Mg in Mg/Nb multilayered nanolaminates studied using synchrotron X-ray diffraction, J. Appl. Phys. 126 (2) (2019) 025302.
[109] K.Y. Yu, Y. Liu, S. Rios, H. Wang, X. Zhang, Strengthening mechanisms of Ag/Ni immiscible multilayers with fcc/fcc interface, Surf. Coating. Technol. 237 (2013) 269–275.

[110] A.V. Pshyk, E. Coy, M. Kempiński, B. Scheibe, S. Jurga, Low-temperature growth of epitaxial Ti2AlC MAX phase thin films by low-rate layer-by-layer PVD, Mater. Res. Lett. 7 (6) (2019) 244–250.
[111] O. Wilhelmsson, J.P. Palmquist, E. Lewin, J. Emmerlich, P. Eklund, P.O. Å. Persson, H. Högberg, S. Li, R. Ahuja, O. Eriksson, L. Hultman, U. Jansson, Deposition and characterization of ternary thin films within the Ti–Al–C system by DC magnetron sputtering, J. Cryst. Growth 291 (1) (2006) 290–300.
[112] R. Benitez, W.H. Kan, H. Gao, M. O'Neal, G. Proust, A. Srivastava, M. Radovic, Mechanical properties and microstructure evolution of Ti2AlC under compression in 25–1100 °C temperature range, Acta Mater. 189 (2020) 154–165.
[113] Y.C. Zhou, X.H. Wang, Deformation of polycrystalline Ti2AlC under compression, Mater. Res. Innovat. 5 (2) (2001) 87–93.
[114] Z. Zhan, M. Radovic, A. Srivastava, On the non-classical crystallographic slip in Tin+1AlCn MAX phases, Scripta Mater. 194 (2021) 113698.
[115] Z. Zhan, Y. Chen, M. Radovic, A. Srivastava, Non-classical crystallographic slip in a ternary carbide – Ti2AlC, Mater. Res. Lett. 8 (7) (2020) 275–281.
[116] W. Tato, D. Landolt, Electrochemical determination of the porosity of single and duplex PVD coatings of titanium and titanium nitride on brass, J. Electrochem. Soc. 145 (12) (1998) 4173.
[117] X. Li, X. Xie, J. Gonzalez-Julian, J. Malzbender, R. Yang, Mechanical and oxidation behavior of textured Ti2AlC and Ti3AlC2 MAX phase materials, J. Eur. Ceram. Soc. 40 (15) (2020) 5258–5271.